◆ Human Brain Mapping 35:5667–5685 (2014) ◆

Investigating the Tradeoffs Between Spatial Resolution and Diffusion Sampling for Brain Mapping with Diffusion Tractography: Time Well Spent?

Evan Calabrese,[1,2] Alexandra Badea,[1] Christopher L. Coe,[3] Gabriele R. Lubach,[3] Martin A. Styner,[4,5] and G. Allan Johnson[1,2]*

[1]Department of Radiology, Center for In Vivo Microscopy, Duke University Medical Center, Durham, North Carolina
[2]Department of Biomedical Engineering, Duke University, Durham, North Carolina
[3]Department of Psychology, Harlow Center for Biological Psychology, University of Wisconsin, Madison, Wisconsin
[4]Department of Computer Science, University of North Carolina, Chapel Hill, North Carolina
[5]Department of Psychiatry, University of North Carolina, Chapel Hill, North Carolina

Abstract: Interest in mapping white matter pathways in the brain has peaked with the recognition that altered brain connectivity may contribute to a variety of neurologic and psychiatric diseases. Diffusion tractography has emerged as a popular method for postmortem brain mapping initiatives, including the ex-vivo component of the human connectome project, yet it remains unclear to what extent computer-generated tracks fully reflect the actual underlying anatomy. Of particular concern is the fact that diffusion tractography results vary widely depending on the choice of acquisition protocol. The two major acquisition variables that consume scan time, spatial resolution, and diffusion sampling, can each have profound effects on the resulting tractography. In this analysis, we determined the effects of the temporal tradeoff between spatial resolution and diffusion sampling on tractography in the ex-vivo rhesus macaque brain, a close primate model for the human brain. We used the wealth of autoradiography-based connectivity data available for the rhesus macaque brain to assess the anatomic accuracy of six time-matched diffusion acquisition protocols with varying balance between spatial and diffusion sampling. We show that tractography results vary greatly, even when the subject and the total acquisition time are held constant. Further, we found that focusing on either spatial reso-

Additional Supporting Information may be found in the online version of this article.

Contract grant sponsor: NIH; Contract grant numbers: R01 MH091645; P41 EB015897; Contract grant sponsor: NIH (A.B.); Contract grant number: K01 AG041211; Contract grant sponsor: NCRR and ORIP; Contract grant number: RR000167

*Correspondence to: G. Allan Johnson; Center for In Vivo Microscopy, Box 3302 Duke University Medical Center, Durham, NC 27710. E-mail: gjohnson@duke.edu

Received for publication 26 February 2013; Revised 5 June 2014; Accepted 24 June 2014.

DOI: 10.1002/hbm.22578
Published online 5 July 2014 in Wiley Online Library (wileyonlinelibrary.com).

lution or diffusion sampling at the expense of the other is counterproductive. A balanced consideration of both sampling domains produces the most anatomically accurate and consistent results. *Hum Brain Mapp 00:000–000, 2014.* © **2014 Wiley Periodicals, Inc.**

Key words: *Macaca mulatta*; diffusion magnetic resonance imaging; diffusion tensor imaging; connectome; neuroanatomy

INTRODUCTION

Mapping white matter connections in the brain has been a major goal of neuroscientists over the last century. Interest in the so-called "connectome" has peaked recently with the realization that aberrant brain connectivity is involved in a variety of neurologic and psychiatric diseases [Lo et al., 2010; Skudlarski et al., 2010; Sundaram et al., 2008]. Many different techniques have been used to map white matter pathways in ex-vivo human brain specimens, including gross brain dissections, myelin-stained histology (e.g., silver staining, Luxol fast blue), anterograde/retrograde tracer studies [Schmahmann and Pandya, 2009], and, more recently, polarized light imaging [Axer et al., 2011]. Rather than replacing its predecessor, each of these techniques has contributed a valuable new perspective to our overall understanding of white matter architecture. One major shortcoming of these techniques is that they are all inherently destructive to the tissue and do not allow direct visualization of three-dimensional (3D) spatial relationships.

Diffusion tractography, one of the newest additions to the white matter mapping initiative, has the potential to nondestructively map the entire connectome at once [Mori et al., 1999]; however, this technique is not without limitations. Diffusion tractography is susceptible to many types of error that can call its anatomic validity into question [Lazar and Alexander, 2003]. Particularly concerning is the fact that there are many different diffusion tractography imaging protocols, each of which yields different results. It is clear that there is something to be gained from diffusion tractography, but further exploration of the consequences of selecting different diffusion acquisition strategies is needed.

The accuracy of any diffusion tractography method depends on its ability to estimate underlying axonal orientation from discrete measurements of tissue diffusion. Diffusion MRI measures tissue diffusion in the spatial domain (i.e., at each image voxel) and in the diffusion domain (often referred to as q-space) [Callaghan et al., 1988]. Increased spatial sampling is achieved with higher-resolution imaging, and increased q-space sampling is achieved by measuring more diffusion angles, and/or more b-values. Both spatial sampling and diffusion sampling consume acquisition time, so realizable diffusion experiments must strike a compromise between the two.

Fortunately, high spatial sampling and high q-space sampling are usually not required for reconstructing accurate fiber tracks, and there is often a tradeoff between the two [Jahanshad et al., 2010; Zhan et al., 2012a,b]. Increased spatial sampling can reduce intravoxel fiber complexity, while increased q-space sampling can resolve intravoxel fiber complexity [Kim et al., 2006; Tuch et al., 2002]. At very high (theoretical) resolution, where each voxel contains only a single fiber population, fiber orientation can be estimated with simple models like diffusion tensor imaging (DTI) [Basser, 1995]. In this theoretical case, DTI yields equivalent results to more complex q-space sampling schemes [Basser, 2002; Yamamoto et al., 2007]. Larger (and more realistic) imaging voxels are likely to contain some degree of fiber complexity, which can often be resolved with increased q-space sampling and more complex reconstruction techniques like Q-ball imaging (QBI) [Tuch, 2004] or diffusion spectrum imaging (DSI) [Wedeen et al., 2005]. Importantly, some intravoxel fiber architectures, like interdigitating crossing, can only be resolved with higher q-space sampling, and others like bending or kissing fibers can only be resolved with higher spatial resolution [Basser et al., 2000; Tuch et al., 2003]. The degree to which these complex geometries exist in the human brain is still debated [Catani et al., 2012; Jeurissen et al., 2013; Wedeen et al., 2012].

The tradeoff between simplifying intravoxel fiber architecture with image resolution, and resolving it with q-space sampling presents an interesting problem: if the goal is anatomically accurate tractography, is it better to spend scan time on increased spatial resolution or increased q-space sampling? This question is particularly relevant for ex-vivo brain mapping initiatives, including the ex-vivo component of human connectome project [McNab et al., 2013], where advanced imaging protocols are commonly used and anatomic accuracy is essential. In this study, we explore these questions with a combination of computer simulations and ex-vivo imaging of the rhesus macaque brain.

MATERIALS AND METHODS

Diffusion Tractography Simulations

Computer simulations were carried out in MATLAB (MathWorks, Natick, MA) to interrogate the effects of varying spatial and angular resolution diffusion imaging on tractography. We generated two 1×1 cm^2 digital fiber phantoms, a circularly curved fiber phantom with thickness 0.5 cm (radius 0.5–1 cm) and an intravoxel crossing

TABLE I. Acquisition details for the six diffusion imaging protocols used in this study

Name	DTI-12	QBI-30	QBI-60	QBI-120	DSI-124	DSI-257
# Directions	12	30	60	120	124	257
# b-values	1	1	1	1	13	22
Isotropic resolution (mm)	0.13	0.2	0.3	0.4	0.4	0.6
Max b-value (s/mm^2)	1,500	4,000	4,000	4,000	10,000	10,000
δ (ms)	4	4.7	4.7	4.7	44.9	44.9
Δ (ms)	14	26	26	26	5.2	5.2
TE (ms)	21.9	32.1	32.1	32.1	51.4	51.4
Acquisition matrix	590 × 444 × 394	384 × 288 × 256	256 × 192 × 176	192 × 144 × 128	192 × 144 × 128	128 × 96 × 88
b0 SNR	62	60	96	131	65	127
bmax SNR	48	38	50	58	17	30

fiber phantom consisting of the same circular curve and a 3.5-mm thick diagonal crossing bundle (crossing angle 60°–90°). Noiseless diffusion weighted image sets were simulated for each of five different gradient schemes (12–120 directions) at 1-μm resolution using a multiple Gaussian diffusion model as described in previous work [Barmpoutis et al., 2009]. Images were then down sampled to reflect varying isotropic acquisition resolutions (0.5–0.1 mm) and corrupted with Rician noise to yield a b0 signal-to-noise ratio (SNR) of 30 in all cases. Although SNR typically varies with acquisition resolution, we used constant SNR for simulations to isolate the effects of varying angular and spatial resolution. Similar simulations accounting for the effects of SNR were also performed and are included as Supporting Information. For these supplementary simulations, SNR was adjusted to be proportional to voxel volume. Diffusion dataset reconstruction and tracking were performed as described later in this section.

Brain Specimens

Two fixed rhesus macaque brains were obtained from the Wisconsin National Primate Research Center at the University of Wisconsin-Madison. The brain specimens were from adult animals that were euthanized humanely by veterinary staff for non-neurological reasons. Following necropsy and tissue extraction by a trained pathologist, the brains were immersed in 10% neutral buffered formalin doped with 1% (5 mM) gadoteridol (ProHance, Bracco Diagnostics, Milan, Italy). Three weeks prior to imaging, specimens were transferred to a 0.1 M solution of phosphate buffered saline doped with 0.5% (2.5 mM) gadoteridol. Immediately prior to imaging, specimens were placed in custom-made MRI-compatible tubes and immersed in Galden low-viscosity perfluoropolyether for susceptibility matching and to prevent specimen dehydration (Solvay Plastics, Brussels, Belgium).

MR Imaging

Imaging was performed on a 7 Tesla small animal MRI system (Magnex Scientific, Yarnton, Oxford, UK) equipped with 650 mT/m Resonance Research gradient coils (Resonance Research, Billerica, MA), and controlled with an Agilent Direct Drive console (Agilent Technologies, Santa Clara, CA). RF transmission and reception were achieved with a 65-mm inner-diameter quadrature RF coil (M2M Imaging, Cleveland, OH). Brain specimens were imaged using each of six time-matched q-space sampling schemes. Each scheme was realized with a 3D spin-echo pulse sequence. Repetition time was held constant at 100 ms to ensure that regardless of the acquisition protocol, a single line of 3D k-space was acquired per TR. Diffusion preparation was accomplished using a pair of unipolar, half-sine diffusion gradient waveforms. The range of acquisition parameters included spatial resolution from 0.13 to 0.6 mm isotropic, angular sampling from 12 to 257 directions, and b-value sampling from one to 22 b-values. One b0 volume was collected for each protocol. Scan time was held constant at 60 h ± 5%. The details of each acquisition strategy are provided in Table I. Complete diffusion datasets and gradient tables from all six protocols are available in the online Supporting Information (http://www.civm.duhs.duke.edu/2013_macaque_tractography/).
In addition to diffusion datasets, a single high-resolution (50-μm isotropic) anatomic image volume was acquired using a 3D gradient echo pulse sequence (repetition time (TR)/echo time (TE) = 50ms/7.2ms).

Diffusion Data Reconstruction and Tractography

Diffusion data were reconstructed in Diffusion Toolkit (http://trackvis.org) using the most appropriate algorithm for the chosen q-space sampling scheme. The 12 direction scheme (DTI-12) was reconstructed using a single-tensor least-squares estimation [Basser and Pierpaoli, 1996]. The 30, 60, and 120-direction schemes (QBI-30, QBI-60, and QBI-120, respectively) were reconstructed with the spherical harmonic basis implementation of Q-ball [Descoteaux et al., 2007; Hess et al., 2006]. The two multi-b-value schemes, DSI-127 and DSI-257, were reconstructed using the DSI Fourier transform approach [Wedeen et al., 2005]. Fiber orientations were estimated from orientation distribution function (ODF) maxima without the use of ODF sharpening techniques.

Whole-brain diffusion tractography was carried out in Diffusion Toolkit (http://trackvis.org) using the FACT (for DTI) or FACT-like (for Q-ball and DSI) tracking algorithm [Mori et al., 1999]. Tracking parameters included an intravoxel turning angle threshold of $< 30^\circ$ and a length threshold of > 5 mm. We chose not to use a fractional anisotropy threshold to facilitate tractography comparisons across different reconstruction methods. Tracks were spline filtered using a one-voxel step length to smooth tracts and eliminate improbable tract geometry.

Primate Brain Track Segmentation

We conducted tractography on two "simple," two "intermediate," and four "complex" fiber pathways in the primate brain. Simple fiber pathways included the anterior commissure (AC), and the optic tracts (OT). These pathways have no major fiber crossings or complex curvature. Intermediate pathways included the cingulum bundle (CB) and the corticospinal tracts (CT). These pathways have central bundles that are relatively simple, but also have major fiber crossings or complex curvature. Complex pathways included the extreme capsule (EmC), the inferior longitudinal fasciculus (ILF), the middle longitudinal fasciculus (MdLF), and the uncinate fasciculus (UF). These long cortical association pathways have complex anatomy with frequent fiber crossings and are known to be difficult to reconstruct with tractography [Schmahmann et al., 2007]. Segmentation was achieved by placing a single region of interest (ROI) disc in the anatomic center of the fiber pathway and accepting only tracks passing through the disc at angles less than 30°. In some cases, obvious stray fibers were manually removed.

Tract-Based Comparisons with Known Anatomy

Unfortunately, there is no universally accepted anatomic "gold standard" for mapping axonal projections in the primate brain, particularly in 3D. This lack of a "gold standard" highlights both the difficulty in validating diffusion tractography, and the scientific need to do so. There is, however, a large collection of autoradiographic connectivity data on the primate brain [Schmahmann and Pandya, 2009]. Autoradiographic connectivity data are not ideal for comparison because they lack a 3D picture of white matter structure; however, they do allow unbiased anatomic validation against a non-tractography-based technique. We performed qualitative comparisons between known anatomy, as defined by autoradiography, and the six diffusion tractography datasets generated for this study. Tract similarity was evaluated based on length, course, and branching pattern.

Quantitative Comparisons Between Tractography Datasets

In addition to qualitative comparisons with known anatomy, we performed quantitative comparisons between tractography datasets. Maximum, and average track length, as well as total track volume, were recorded for each dataset. Differences between tractography datasets were further evaluated using track density images (TDIs). TDIs were generated for each tractography dataset at the native acquisition resolution to ensure a consistent tractography seeding pattern (i.e., one seed per voxel). TDIs were then resampled to 130-μm isotropic resolution using nearest neighbor interpolation to allow direct comparison between protocols. For each white matter pathway included in the analysis, a mean TDI was generated by averaging TDIs from all six acquisition protocols. Individual TDIs were then compared to the average using normalized cross-correlation. This comparison did not assess anatomic accuracy directly, but rather assessed consistency between different tractography datasets.

RESULTS

Tractography Simulations

We first used tractography simulations (Figs. 1 and 2) to determine the effects of varying angular and spatial resolution on diffusion tractography. Simulated fiber tracts are colored on the basis of the angle of the line defined by the two endpoints of each track relative to the vertical direction, where green specifies 0° and red specifies 90°. Both phantoms were designed such that the line connecting the endpoints of all fibers was at a 45° angle relative to vertical; thus, all correct tracks should appear yellow (equal parts red and green in RGB color space).

The curve phantom (Fig. 1) represents a relatively simple tractography target. There are two major tractography errors evident in these simulations. First, low spatial resolution datasets (left side of figure) yielded several short and prematurely terminating tracks near the edges of the fiber bundle. These errors are likely the result of partial volume averaging, as they are present in all angular sampling schemes and are diminished at higher spatial resolution. Second, the combination of high spatial and low angular resolution (i.e., bottom right of figure) caused virtually all tracks to terminate prematurely. Increasing angular resolution, or decreasing spatial resolution, yielded a lower proportion of prematurely terminating tracks. This effect is likely the result of minor errors in the primary fiber orientation that accumulate as the propagating tractography streamline passes through multiple voxels [Lazar and Alexander, 2003].

The crossing phantom (Fig. 2) shows a similar pattern of premature fiber termination on the edges of fiber bundles, particularly in lower spatial resolution datasets. The fiber crossing was relatively well resolved in all datasets except the 12 and 30-angle datasets. The 30-angle datasets had only minor errors that caused tracks to prematurely terminate within the crossing region. These errors were more apparent at higher spatial resolutions, presumably because there are simply more voxels within the crossing region at

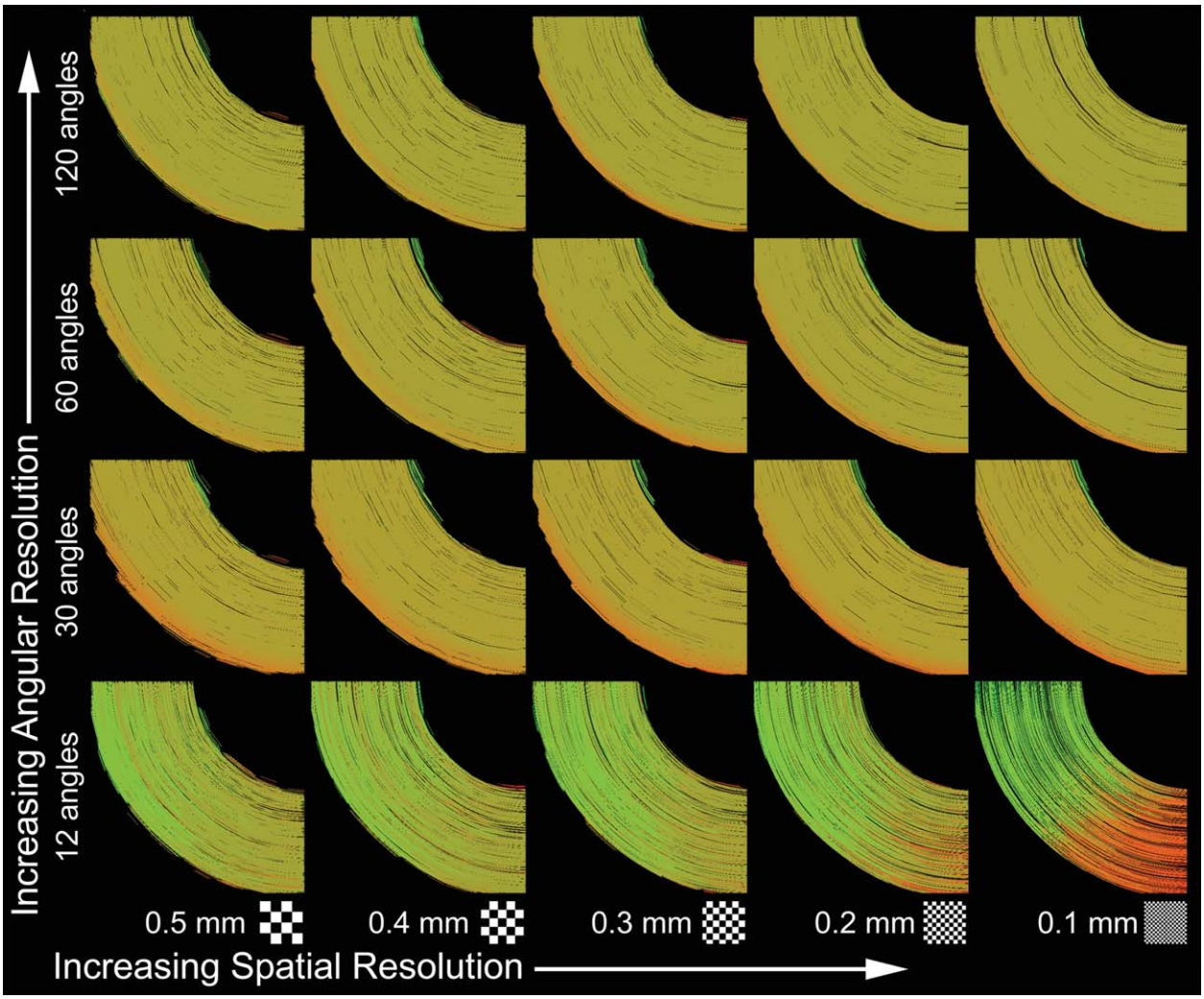

Figure 1.

Curved fiber phantom tractography simulations showing the effects of varying angular and spatial resolution. Each track is colored based on the angle of the line connecting its endpoints relative to vertical, with red = 90° and green = 0°. The phantom was designed such that the line connecting the endpoints of each fiber is at 45° relative to vertical, thus correct tracks appear yellow (equal parts red and green in RGB color space). Checkerboard voxel grids are included at the bottom of each column to show voxel size. [Color figure can be viewed in the online issue, which is available at wileyonlinelibrary.com.]

higher resolution. The 12-angle dataset suffered from both premature termination and erroneous turning in the crossing region, and these errors were present at all spatial resolutions. It is important to note that the 12-angle datasets were reconstructed as a tensor, so resolving more than a single fiber population per voxel is not possible. Nonetheless, the 12-angle sampling scheme was included in the crossing phantom analysis for completeness and to demonstrate the type of errors that occur when tensor reconstruction is used on complex fiber geometry.

Both the curve and crossing phantom simulations were also carried out accounting for the interdependency of SNR and voxel volume, and are included as supplemental Figures 1 (curve phantom) and 2 (crossing phantom). In these simulations, SNR values below ~30 lead to noticeable tractography errors. These data demonstrate that SNR can only be sacrificed for increased spatial resolution up to a point, after which SNR-induced errors predominate.

Ex-Vivo Primate Brain Imaging Schemes

The six time-matched q-space sampling schemes used for this ex-vivo macaque tractography analysis are described more completely in Table I and Figure 3. Table I lists all of the relevant acquisition parameters for each protocol as well

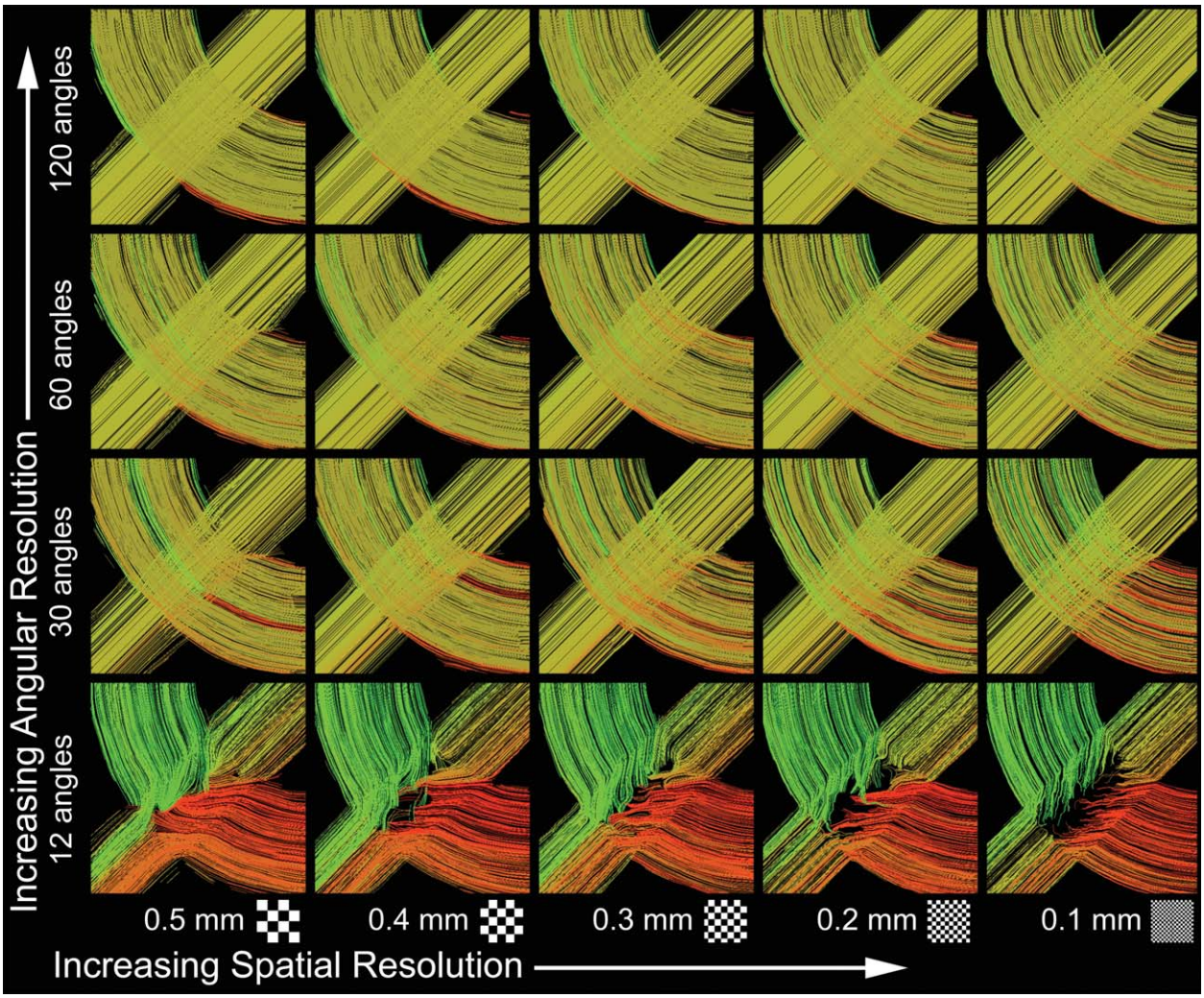

Figure 2.

Crossing fiber phantom tractography simulations showing the effects of varying angular and spatial resolution. Crossing angle varies from 60° to 90° within the phantom. Each track is colored based on the angle of the line connecting its endpoints relative to vertical, with red = 90° and green = 0°. The phantom was designed such that the line connecting the endpoints of each fiber is at 45° relative to vertical, thus correct tracks appear yellow (equal parts red and green in RGB color space). Checkerboard voxel grids are included at the bottom of each column to show voxel size. [Color figure can be viewed in the online issue, which is available at wileyonlinelibrary.com.]

as the SNR for the b0 and maximum diffusion weighted image (bmax). SNR was measured as the ratio of the signal average in a cortical ROI and the standard deviation of a large area of background noise. Measured SNR values are in excess of general recommendations for the respective q-space sampling scheme [Descoteaux et al., 2007; Farrell et al., 2007; Hess et al., 2006; Tuch, 2004; Wedeen et al., 2005] and are comparable to previous ex-vivo work in the macaque brain [D'Arceuil et al., 2007; Rane et al., 2010; Wedeen et al., 2008]. Figure 3 highlights the sampling differences between protocols in both the spatial and q-space domains. Higher spatial resolution was achieved at the cost of decreased q-space sampling and vice versa such that the scan time remained constant between protocols. Partial volume effects at gray matter and white matter borders are readily apparent in the lower spatial resolution schemes and are virtually absent in the higher-resolution DTI-12 scheme. Additionally, there are minor variations in the image contrast due to echo time differences between the different protocols.

Ex-Vivo Primate Tractography Results

The following sections and corresponding figures (Figs. 4–11) present a comparison of tractography results from the time-matched diffusion sampling protocols described

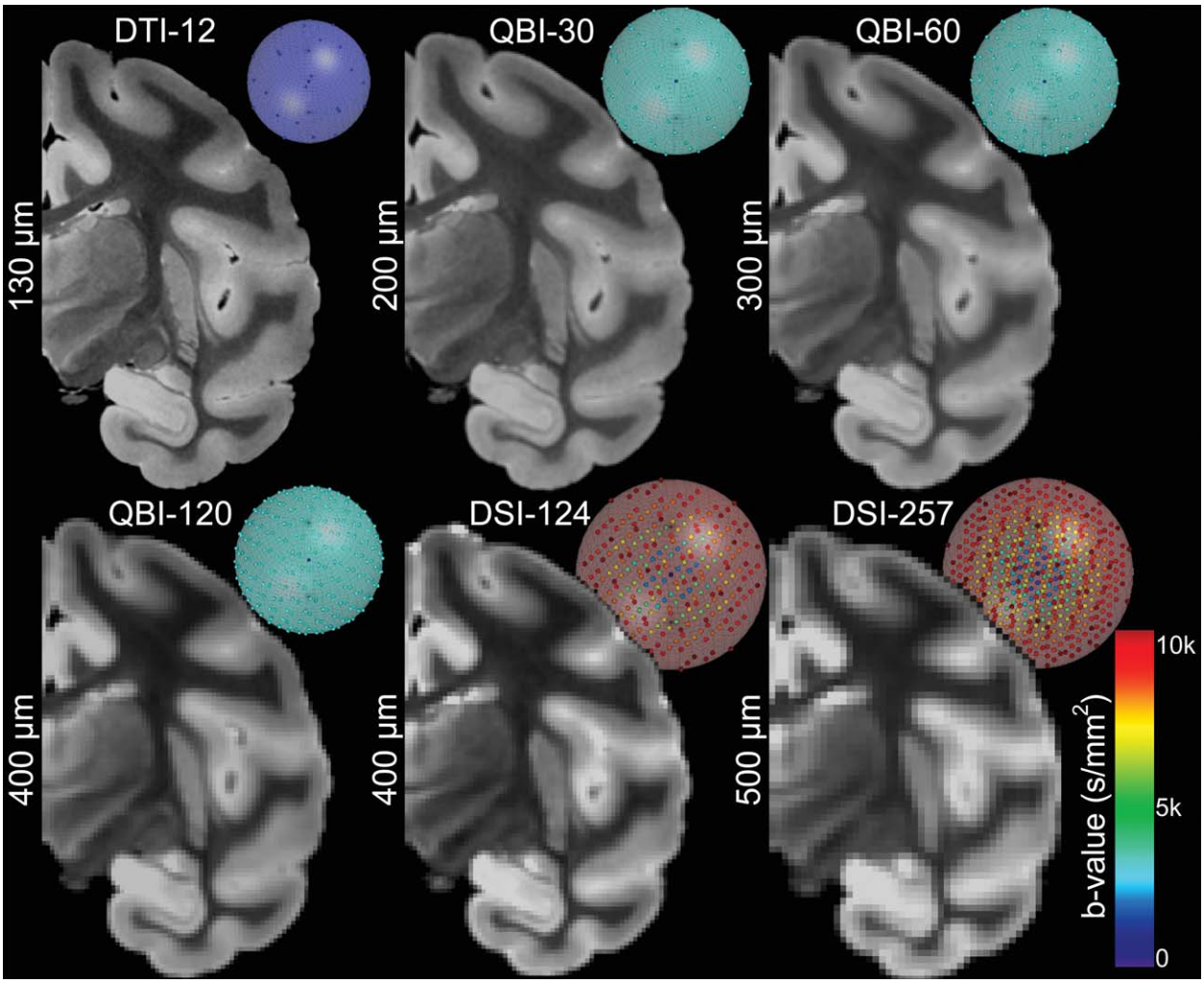

Figure 3.

Visualization of spatial sampling and q-space sampling in each of the six time-matched diffusion MRI protocols used in this study. For each protocol, the left half of a single coronal slice from the b0 image is shown along with a diagram of the q-space sampling scheme. The color (see legend) and radius of each q-space diagram indicates b-value, and each point represents a single measurement in q-space. Acquisition resolution is indicated to the left of each image. [Color figure can be viewed in the online issue, which is available at wileyonlinelibrary.com.]

in Table I. In each case, directionally colored tractography images from all six protocols are displayed side-by-side along with a single slice from the corresponding b0 image. Slice location is indicated in the top-left corner of each figure with a plane intersecting a 3D surface rendering of the macaque brain. The relevant diagrams from an autoradiography-based fiber pathway atlas are included for anatomic reference (by permission of Oxford University Press) [Schmahmann and Pandya, 2009]. Autoradiography diagrams were not available for AC, CT, and OT, so high-resolution anatomic images are displayed instead. Additional views of all tracks are included as Supporting Information (http://www.civm.duhs.duke.edu/2013_macaque_tractography/).

Simple Fiber Pathways

Anterior commissure

The AC is a compact bundle of fibers that, along with the corpus callosum, is a major pathway for interhemispheric connections (Fig. 4). The AC crosses the midline immediately rostral to the fornix and superior to the basal forebrain. The large posterior limbs of the AC connect the bilateral superior and inferior temporal lobes. The considerably smaller anterior limbs form a U-shaped bundle that extends rostrally connecting various olfactory structures. The anterior and posterior limbs of the AC can be clearly seen in the magnified inset of the anatomic image presented in the bottom left panel of Figure 4. Tractography

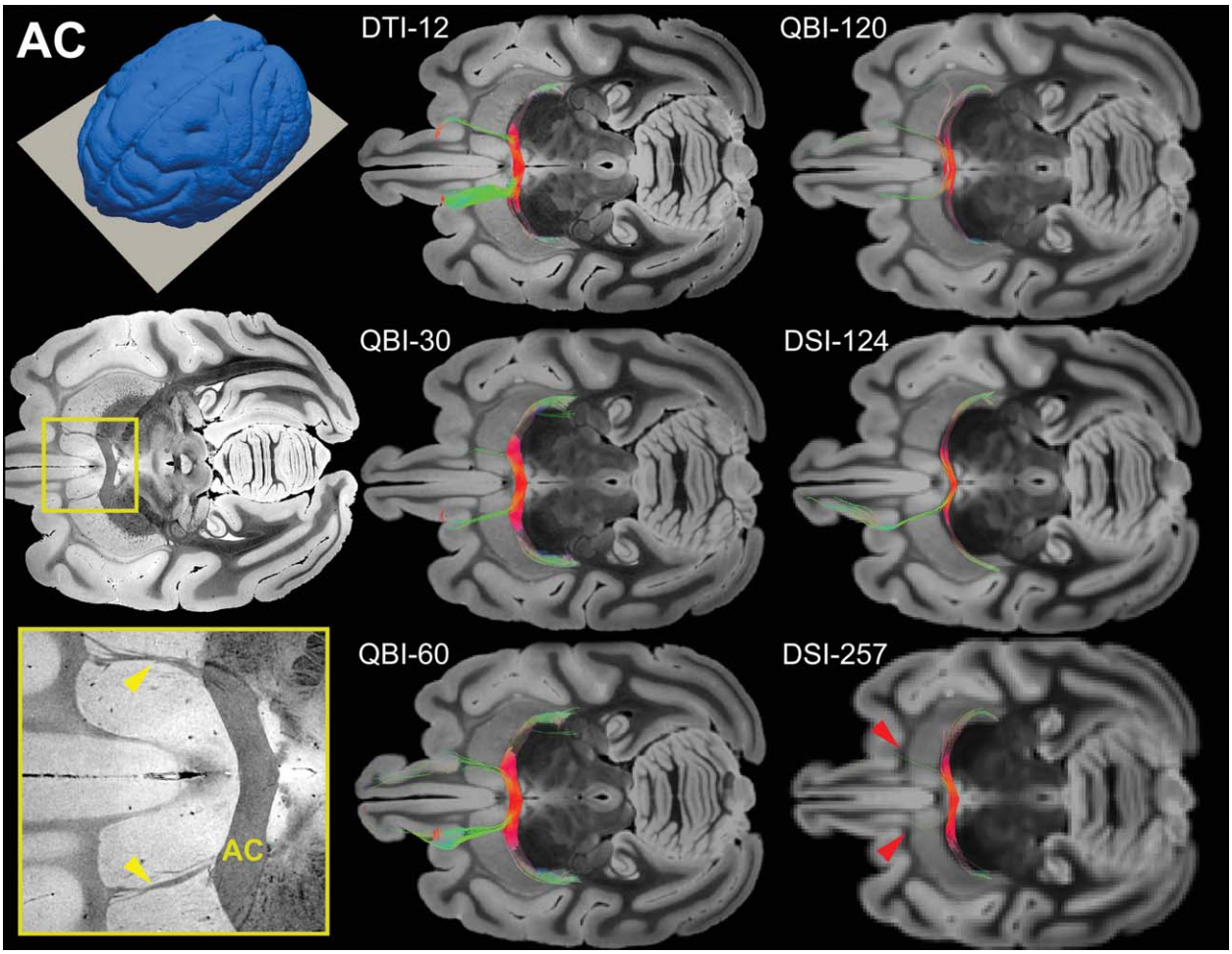

Figure 4.

Anterior commissure (AC) tractography results. Tractography in this "simple" pathway was qualitatively similar across protocols, with the exception of the small anterior limbs (anatomic image, yellow arrowheads). Low spatial resolution datasets had small or absent anterior limbs (e.g. DSI-257, red arrowheads), presumably due to partial volume effects. [Color figure can be viewed in the online issue, which is available at wileyonlinelibrary.com.]

in this relatively simple fiber pathway was fairly consistent across all acquisition protocols. The major difference between protocols was the thickness of the posterior limbs and presence or absence of the anterior limbs. Higher spatial resolution datasets (DTI-12, QBI-30, QBI-60) had thicker posterior limbs and more well-defined anterior limbs. In contrast, lower-resolution datasets with higher q-space sampling had thinner posterior limbs and small or absent anterior limbs. Overall higher spatial resolution datasets were more representative of known anatomy.

Optic tracts

The OT (Fig. 5) forms the middle portion of the visual system and courses between the optic chiasm and the lateral geniculate nucleus (LGN). The LGN sits just rostral to the hippocampal formation at the lateral side of the thalamus as shown in the high-resolution anatomic image (Figure 5, bottom left). Tractography of the OT was very consistent across all six acquisition protocols. All six datasets correctly connected the LGN and represented midline crossings in the optic chiasm. The DTI-12 dataset had slightly more stray tracks than other datasets but still closely represented known anatomy. Overall differences between protocols were minimal for the OT and no dataset was significantly better than the others.

Intermediate Fiber Pathways

Cingulum bundle

The CB courses rostrocaudally immediately dorsal to the corpus callosum and connects the orbital-frontal,

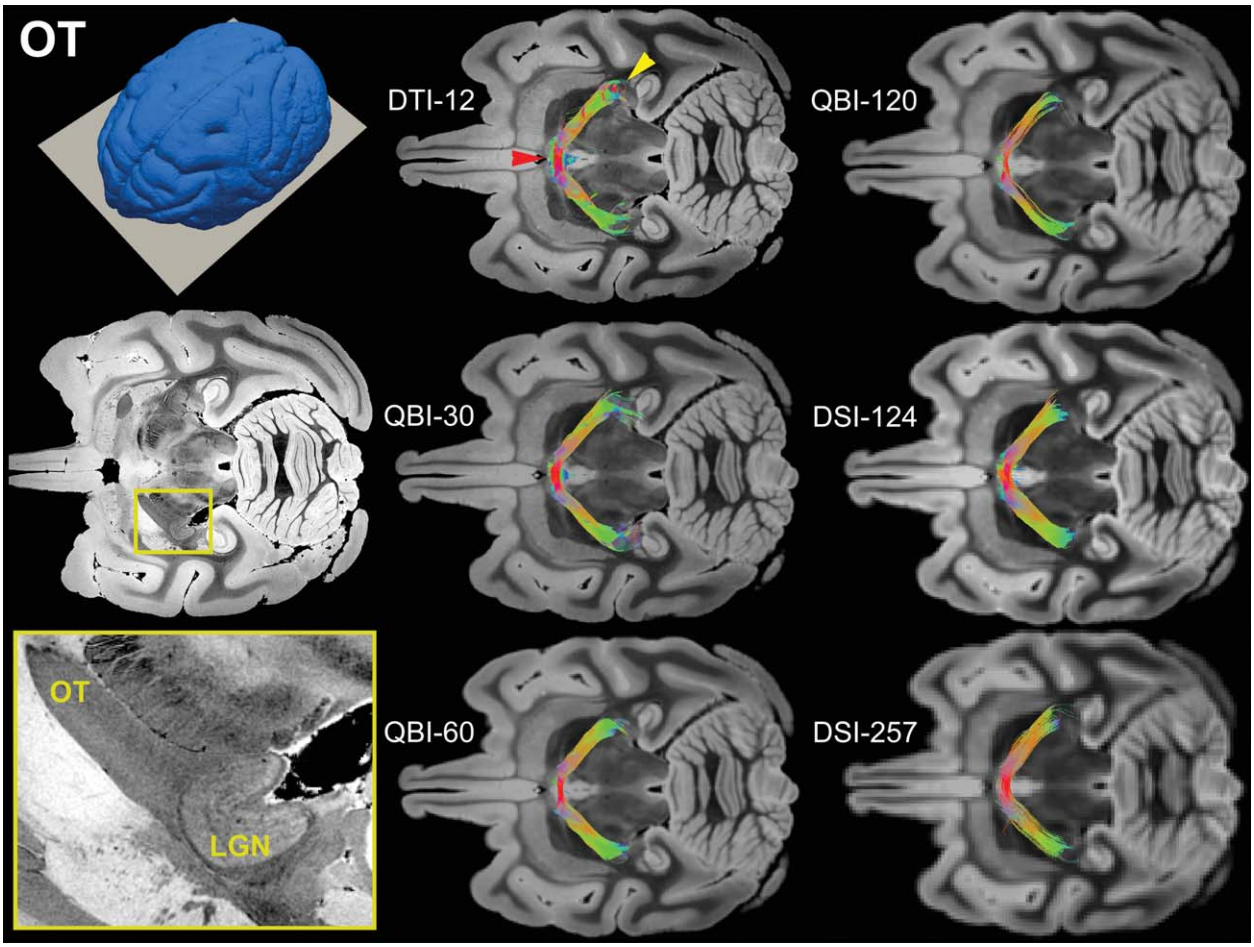

Figure 5.

Optic tract (OT) tractography results. Tractography was qualitatively very similar across protocols in this "simple" pathway. All six protocols correctly represented the optic chiasm midline crossing (e.g. DTI-12, red arrowhead) and extended to the lateral geniculate nucleus (LGN) (e.g. DTI-12, yellow arrowhead). [Color figure can be viewed in the online issue, which is available at wileyonlinelibrary.com.]

prefrontal, cingulate, parietal, and temporal cortices (Fig. 6). All six tractography datasets were able to reconstruct nearly the full rostrocaudal extent of the CB, but the branching pattern differed substantially between datasets. The rostral-most branches to the prefrontal and orbitalfrontal cortices were more correctly represented by QBI-120 and DSI-124 and were largely absent from other datasets. Although DTI-12 appears to have a prefrontal branch, these tracks curve dorsally and medially and may be largely erroneous. Many of the tractography datasets picked up dorsally oriented cingulate cortex U-fibers along the major limb of the CB to varying degrees. DTI-12 picked up the most U-fibers while DSI-256 had none. All six datasets tracked the small dorsal branch connecting the caudal parietal cortex (area Opt); however, DTI-12 and QBI-30 had several erratic stray fibers emerging from this branch. The major caudal branch connecting retrosplenial areas 29 and 30 was present in all datasets, but the larger branch, which extends ventrally into the temporal lobe, was absent from all six datasets.

Corticospinal tracts

The CT are formed by axons from upper motor neurons in the primary motor cortex (Fig. 7). These fibers course caudally and ventrally from the motor cortex, through the internal capsulae, the cerebral peduncles, and the pyramids before decussating and terminating in the spinal cord. The internal capsule portion of the CT is shown in high-resolution anatomic image in the bottom left panel of Figure 7. The subcortical portion of the CT was well represented by all six tractography datasets, but cortical tracks varied considerably. Although CT fibers originate from the length of the primary motor cortex, only the superior-most fibers were reconstructed in tractography datasets. Interestingly, bilateral cortical tracks were only correctly represented in

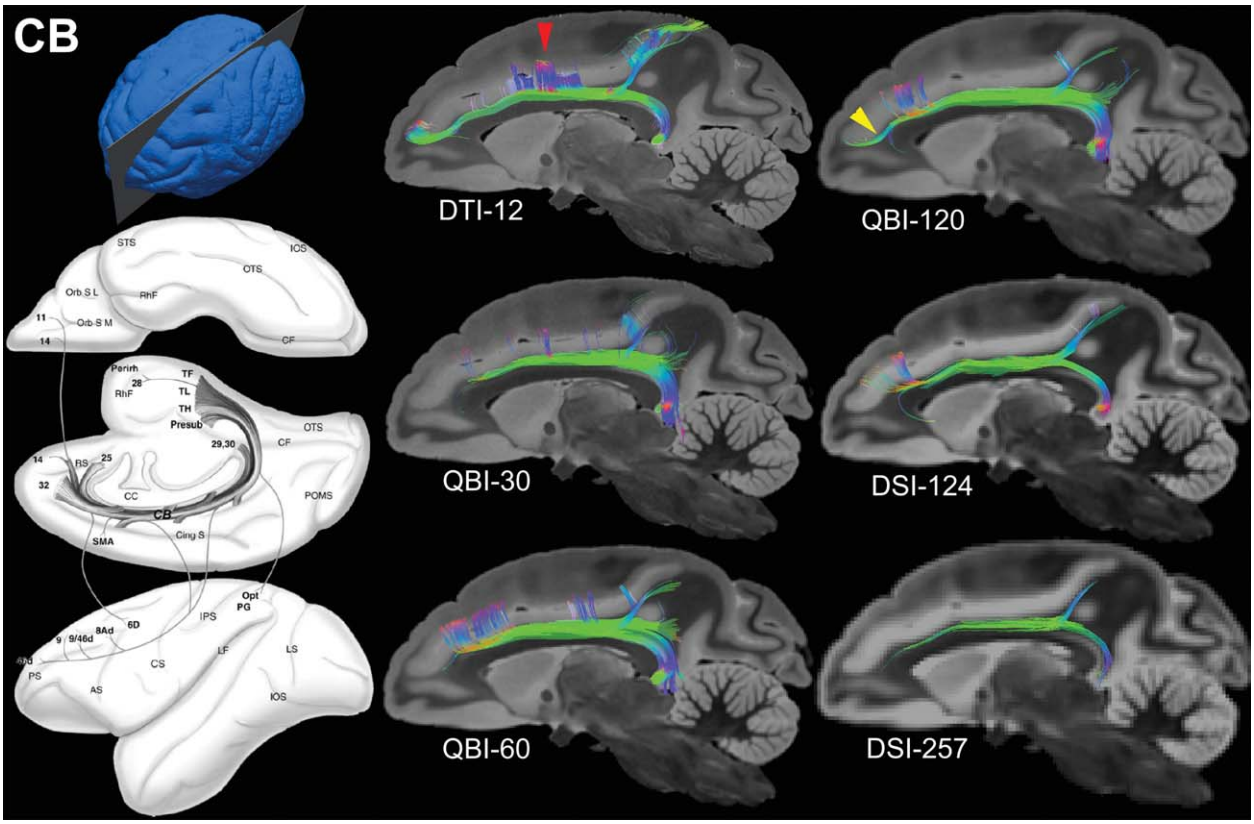

Figure 6.

Cingulum bundle (CB) tractography results. This "intermediate" pathway has a relatively simple central bundle, but also features distal branching with complex curvature. For example, the rostral-most branches to the prefrontal and orbital-frontal cortices (QBI-120, yellow arrowhead) were only present in QBI-120 and DSI-124. Some datasets erroneously tracked dorsally oriented cingulate cortex U-fibers (e.g. DTI-12, red arrowhead). [Color figure can be viewed in the online issue, which is available at wileyonlinelibrary.com.]

the high spatial resolution DTI-12 and QBI-30 datasets. Lower-resolution datasets with higher q-space sampling had unilateral or completely absent cortical tracks. In these datasets, premature termination occurred near the convergence of several other fiber bundles including the frontooccipital fasciculus (FOF), the superior longitudinal fasciculus II (SLF II), the striatal bundle (StB), and the subcallosal fasciculus of Muratoff (MB). It is presumed that partial volume contributions from these other pathways lead to erroneous fiber orientation estimation in low spatial resolution datasets. Supporting Information, Figure 3 provides visualizations of the estimated fiber orientations in the premature termination area for both the QBI-30 and QBI-120 datasets.

Complex Fiber Pathways

Middle longitudinal fasciculus

The MdLF forms the major white matter component of the superior temporal gyrus and courses between the caudal inferior parietal lobule and the superior temporal sulcus (Fig. 8). All six protocols were able to approximate nearly the full extent of the pathway; however, DTI-12 and DSI-257 were slightly shorter than the other four datasets. This difference is reflected in the mean length measurements in Table II, which shows that DTI-12 and DSI-257 are several millimeters shorter than other datasets. The degree of stray tracks appeared to decrease with increasing q-space sampling, with DTI-12 having the most stray fibers, and DSI-257 having almost none. The branching pattern at the ventral terminus of the MdLF was well represented by the three QBI protocols and DSI-124, but was less apparent in DTI-12 and DSI-257. No single dataset clearly stood out as the most similar to known anatomy, but QBI-60, QBI-120, and DSI-124 each had very similar length, course, and branching patterns with relatively few stray fibers.

Inferior longitudinal fasciculus

The ILF is a particularly long association pathway that connects the temporal lobe with the occipital lobe, caudal

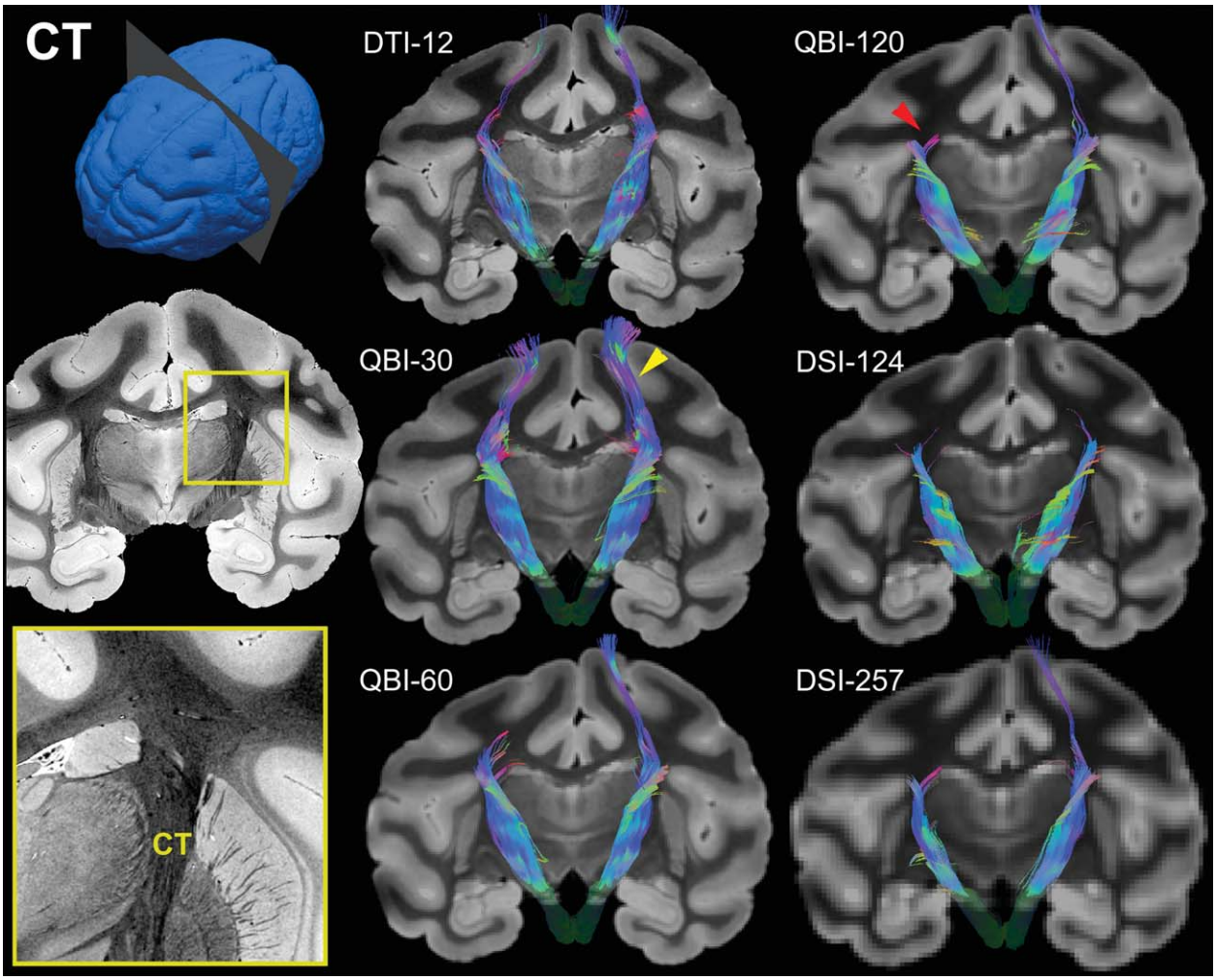

Figure 7.

Corticospinal tract (CT) tractography results. This "intermediate" pathway has a relatively simple posterior course, but features a major crossing with horizontally oriented callosal fibers (as shown in magnified inset of anatomic image). This crossing was a major source of error (e.g. QBI-120, red arrowhead). Only the two highest spatial resolution protocols correctly extended bilaterally into the primary motor cortices (e.g. QBI-30, yellow arrowhead). [Color figure can be viewed in the online issue, which is available at wileyonlinelibrary.com.]

parietal cortex, and caudal cingulate gyrus (Fig. 9). Despite its length, tractography was relatively successful at reconstructing the ILF. The ventral limb, which courses through the temporal lobe white matter, was accurately reconstructed by all diffusion protocols except DTI-12, where the ventral tracks followed a tortuous path, eventually straying rostrally into the superior temporal gyrus. The dorsal branches connecting the parietooccipital area (POa), caudal parietal cortex (area Opt), and dorsal prelunate area (DP) were missing in the DSI protocols, but were present to varying degrees in the three QBI protocols. Interestingly, all six protocols correctly reconstructed the small branch of the ILF that extends into the ventral preoccipital areas (i.e., V4V and V3V). Overall, the three QBI datasets appeared closest to the known anatomy with the major difference between datasets being the dorsal branching pattern.

Uncinate fasciculus

The UF connects the rostral and ventral temporal regions with the medial and orbital-frontal cortices (Fig. 10). Tractography results for the UF were quite similar across the six protocols used for this study. The DTI-12 protocol yielded the most stray fibers, but was otherwise similar to other datasets. The major difference between datasets was the representation of the rostral limb extending into the medial and orbital-frontal cortices. Although no tractography dataset extended as far rostrally as

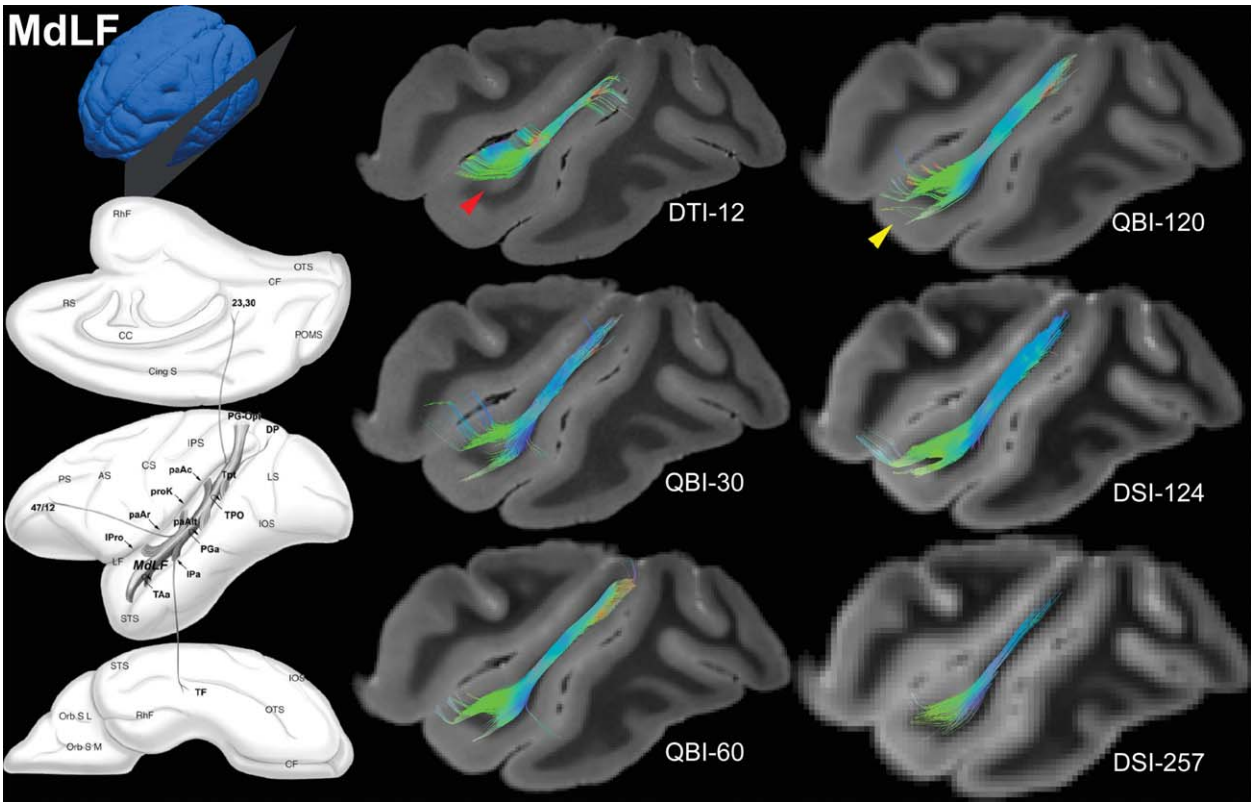

Figure 8.

Middle longitudinal fasciculus (MdLF) tractography results. This "complex" cortical association pathway features many fiber crossings, which resulted in premature termination and stray fibers in low diffusion sampling datasets (e.g. DTI-12, red arrowhead). The ventral branching pattern of the MdLF (e.g. QBI-120, yellow arrowhead) was well represented by all datasets except DTI-12 and DSI-257. [Color figure can be viewed in the online issue, which is available at wileyonlinelibrary.com.]

autoradiography data indicate, the two DSI protocols extended the farthest medially and rostrally into the frontal lobe.

Extreme capsule

The EmC connects the superior temporal region caudally with the prefrontal and orbital-frontal cortices rostrally (Fig. 11). Autoradiography data suggest that the rostral portion of this fiber pathway forks into a superior ramus, which courses into the prefrontal cortex, and an inferior ramus, that connects to the orbital-frontal cortex. The EmC courses very close to a sheet-like group of cortical U-fibers in the frontal cortex, and the resulting aberrant tracking of these U-fibers was a major source of error in these tractography results. The DTI-12 dataset was the worst affected, with virtually all tracks curving laterally into the cortical U-fiber pathway. The three QBI protocols also had significant U-fiber involvement, although in each case at least some tracks continued correctly into the prefrontal cortex. Neither of the two DSI datasets had any significant cortical U-fiber involvement. The rostral branching pattern differed significantly between datasets. The inferior ramus connecting the orbital-frontal cortex was not present in any dataset. The larger superior ramus connecting the dorsal prefrontal cortex was present in QBI-60, DSI-124, and DSI-257, but was absent or truncated in the other three datasets.

Quantitative Comparisons Between Tractography Datasets

Tractography length and volume statistics are presented in Table II. In most cases, mean track length was similar for all six acquisition schemes; however, track volume varied by an order of magnitude in some cases. In general, the length and volume statistics from the DTI-12 scheme were most different from other schemes. This observation is supported by the results of the mean track correlation analysis (Fig. 12). DTI-12 tractography was, on average, the most different from mean tractography across the eight pathways included in our analysis. There was a general trend toward increasing similarity with other datasets as q-space

TABLE II. Length and volume statistics for tractography data

		Max length (mm)	Mean length (mm)	Volume (ml)
AC	DTI-12	46.37	27.84	0.05
	QBI-30	57.31	41.11	0.15
	QBI-60	58.23	36.30	0.21
	QBI-120	44.12	27.28	0.11
	DSI-124	56.51	38.19	0.09
	DSI-257	41.91	31.22	0.18
CB	DTI-12	66.09	26.48	0.17
	QBI-30	43.14	26.20	0.14
	QBI-60	48.35	24.49	0.26
	QBI-120	53.47	29.08	0.28
	DSI-124	50.49	23.43	0.16
	DSI-257	26.40	16.64	0.15
CT	DTI-12	67.40	46.08	0.32
	QBI-30	69.06	47.91	0.79
	QBI-60	66.72	45.55	0.78
	QBI-120	65.21	42.13	0.97
	DSI-124	54.05	39.64	0.92
	DSI-257	57.31	41.76	1.11
OT	DTI-12	41.04	17.21	0.11
	QBI-30	53.72	24.89	0.21
	QBI-60	43.79	23.14	0.18
	QBI-120	38.59	16.27	0.15
	DSI-124	37.23	16.25	0.28
	DSI-257	40.04	17.13	0.32
MdLF	DTI-12	23.17	12.46	0.03
	QBI-30	29.09	17.88	0.06
	QBI-60	31.01	18.86	0.09
	QBI-120	28.28	17.49	0.12
	DSI-124	29.47	16.11	0.15
	DSI-257	18.46	11.25	0.10
ILF	DTI-12	53.53	12.30	0.07
	QBI-30	56.82	24.77	0.17
	QBI-60	61.53	27.43	0.30
	QBI-120	47.23	22.34	0.29
	DSI-124	31.87	17.33	0.20
	DSI-257	34.83	21.47	0.26
UF	DTI-12	22.03	15.26	0.03
	QBI-30	22.05	15.05	0.02
	QBI-60	18.66	10.59	0.05
	QBI-120	23.63	15.50	0.09
	DSI-124	17.37	11.05	0.06
	DSI-257	38.88	13.12	0.14
EmC	DTI-12	66.11	22.62	0.43
	QBI-30	45.04	17.47	0.15
	QBI-60	44.01	19.15	0.32
	QBI-120	45.63	19.95	0.33
	DSI-124	44.04	18.16	0.31
	DSI-257	46.90	22.39	0.63

sampling increased and spatial resolution decreased. QBI-120, DSI-124, and DSI-257 were, on average, the most consistent with other datasets. Importantly, tractography similarity measurements did not directly correlate with the choice of reconstruction protocol.

DISCUSSION

The Effect of Acquisition and Reconstruction Strategies

One of the most interesting, and perhaps concerning, findings to emerge from this study is that tractography results can vary substantially, even in advanced ex-vivo studies of the same subject with fixed total acquisition time. This result is not necessarily surprising, when considering the different acquisition and reconstruction strategies that were used. Indeed, each of the three algorithms used for this study has strengths and weaknesses, which dictate tractography behavior in areas of fiber complexity. This study highlights the problems that can arise when comparing tractography results from different acquisition and fiber estimation strategies. The effect of fiber estimation technique has been more thoroughly explored elsewhere [Catani et al., 2012; Fillard et al., 2011; Wedeen et al., 2012]. The fiber estimation techniques used in this study were chosen to be in line with previous ex-vivo work [McNab et al., 2009; Wedeen et al., 2008]; however, newer methods, such as ODF sharpening, have been shown to improve fiber estimation accuracy, particularly for low-angle fiber crossings [Descoteaux et al., 2009; Yeh and Tseng, 2013; Yeh et al., 2011]. The use of such fiber ODF estimation techniques could change the diffusion sampling requirements for generating anatomically accurate tractography. Interestingly, tractography results were substantially different even between datasets of the same type (i.e., between the three QBI protocols), suggesting that the reconstruction method was not the only factor dictating these differences.

Effects of Tissue Fixation

Formalin fixation produces an approximately fourfold reduction in brain diffusivity [Alexander et al., 2010; Dyrby et al., 2011]. As a result, fourfold larger b-values are required to achieve in-vivo equivalent diffusion weighting. Fortunately, ex-vivo diffusion imaging offers several image quality improvements that improve the ability to estimate fiber orientation [Lerch et al., 2012]. Ex-vivo studies typically have higher SNR, are not complicated by physiologic/subject motion, and avoid EPI-induced eddy current distortions, each of which affect the ability to estimate fiber orientation [Jones, 2004; Le Bihan et al., 2006; Skare and Andersson, 2001]. Previous ex-vivo studies have shown that b-values of 2,000–8,000 s/mm^2 allow consistent estimations of fiber directions with Q-ball, and accurate tensor estimation typically requires even lower b-values [Dyrby et al., 2011]. The optimal b-value for ex-vivo DSI has not been tested directly to our knowledge; however, the b-value used in this study is within the range of previously published ex-vivo DSI studies [de Crespigny et al., 2005].

Formalin fixation also causes an approximately threefold reduction in tissue T2 [Dawe et al., 2009]. In this study, T2

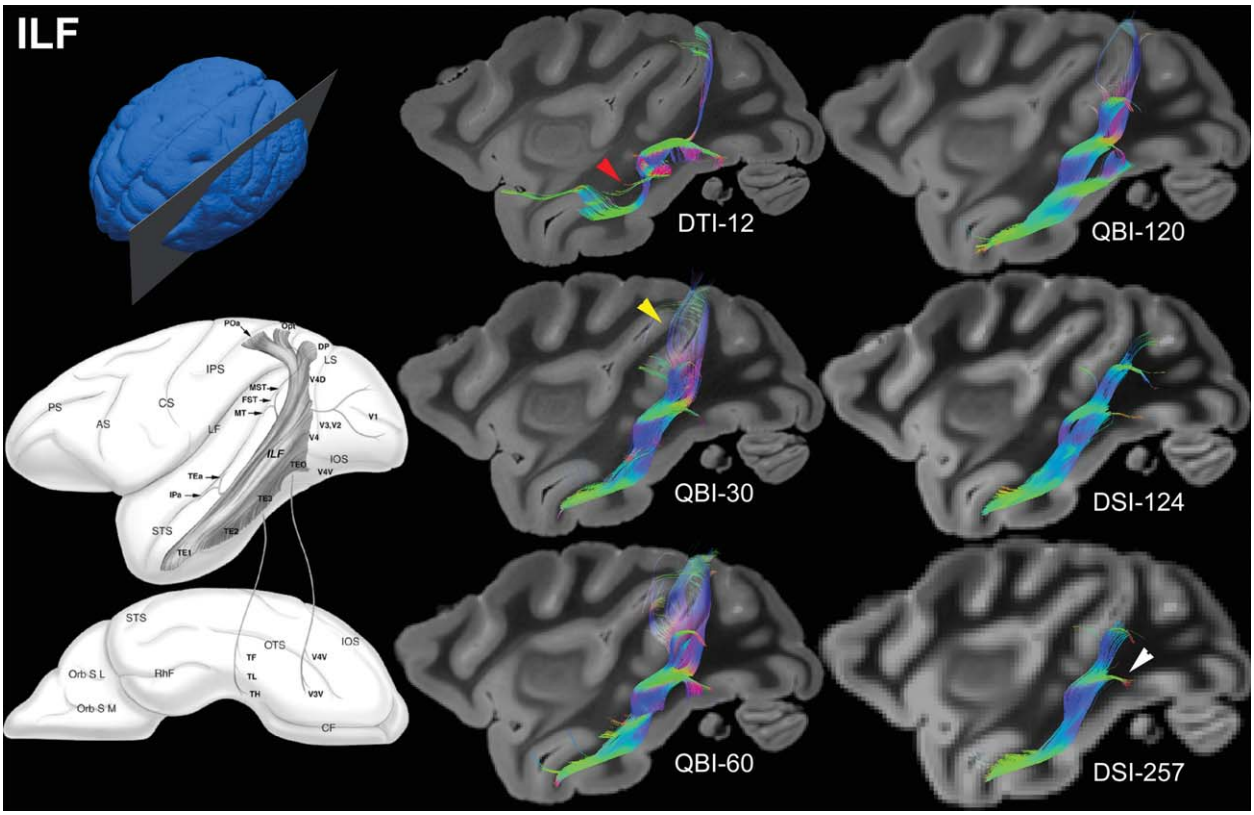

Figure 9.

Inferior longitudinal fasciculus (ILF) tractography results. This long, "complex" pathway has several major fiber crossings, which caused major errors in the DTI-12 dataset (red arrowhead). The thin, dorsal branches connecting the parietooccipital area (POa), caudal parietal cortex (Opt), and dorsal prelunate area (DP) (e.g. QBI-30, yellow arrowhead), were sparse or missing in the lowest spatial resolution datasets. The small branch of the ILF extending into the ventral preoccipital areas was present in all six datasets (e.g. DSI-257, white arrowhead). [Color figure can be viewed in the online issue, which is available at wileyonlinelibrary.com.]

reduction was offset by the use of advanced magnetic field gradients, which allow dramatically shorter diffusion preparation time and, thereby, shorter echo time.

Recommendations for Anatomically Accurate Tractography

Ensuring anatomic accuracy is essential for the future of diffusion tractography studies. Accurate 3D maps of white matter connectivity could allow researchers to assess architectural differences in a quantitative way, and foster the development of automated approaches for identifying signatures of normal versus diseased white matter tracts. Although the results of this study are insufficient to provide a definitive approach to ensuring anatomically accurate tractography, they do shed light on a number of important considerations. We have attempted to distill our observations into a short list of recommendations for getting the most meaningful tractography out of a given acquisition time.

Anatomy matters

It is well known that certain white matter pathways are easy to reconstruct with tractography, and others are not. Structures that are relatively easy to track, such as the curved fiber phantom and the two "simple" pathways chosen for this study, can be accurately reconstructed using simple models like DTI. In contrast, more complex structures, including the crossing fiber phantom and the four "complex" pathways analyzed in this study, require estimation of fiber crossings. The optimal diffusion acquisition strategy thus depends to some degree on the specific anatomy being imaged. Simple fiber pathways, such as the AC and OT, were actually more accurately represented by high-resolution/low-q-space sampling datasets. In these cases, it seems that the reduction in partial volume effects provided by high spatial resolution outweighs the effects of reduced q-space sampling. This effect can be understood intuitively in structures like the anterior limbs of the AC, which are

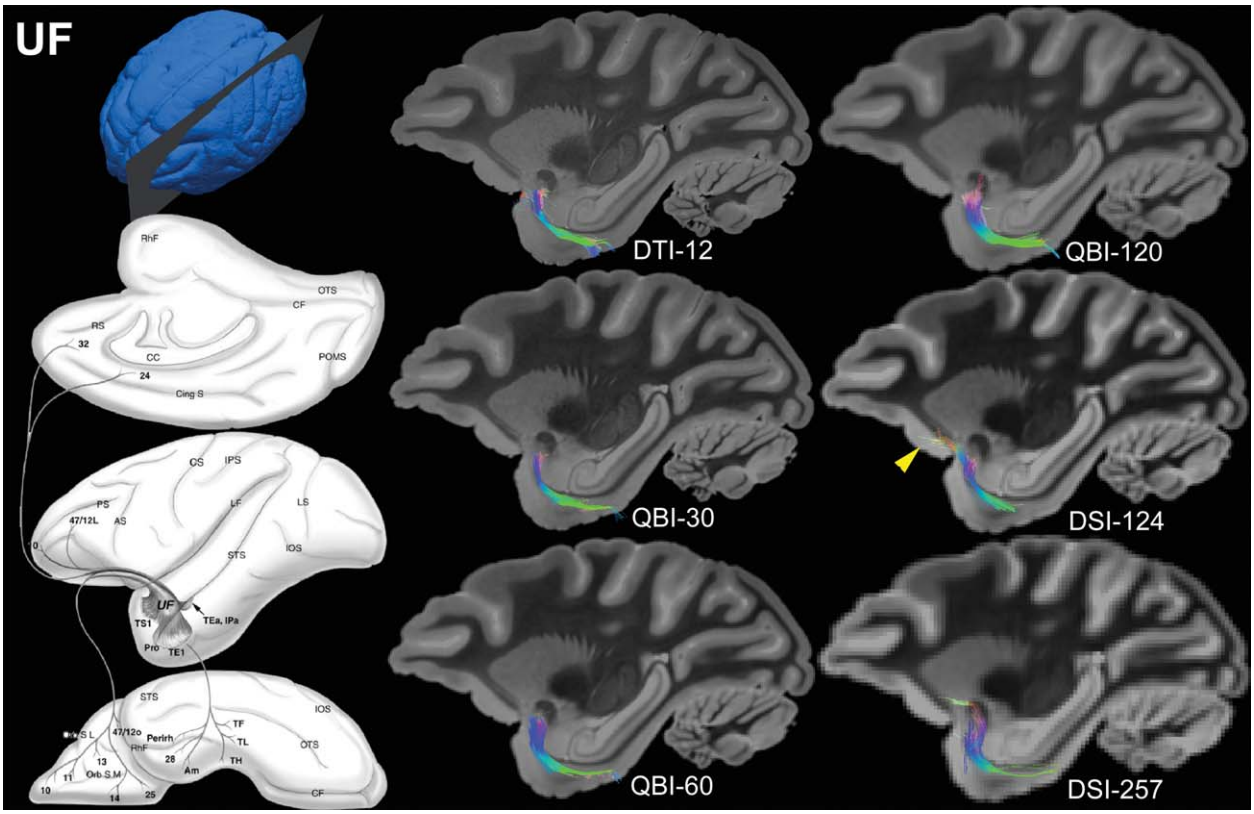

Figure 10.

Uncinate fasciculus (UF) tractography results. Despite the complex curvature and crossings present in this "complex" pathway, all six protocols generated qualitatively similar results. The major difference between datasets was the rostral limb extending into the orbital-frontal cortex, which was only present in the two DSI protocols (e.g. DSI-124, yellow arrowhead). [Color figure can be viewed in the online issue, which is available at wileyonlinelibrary.com.]

straight and coherent, but small and thus vulnerable to partial volume effects. If the tractography target is relatively simple, high spatial resolution may be preferable to high q-space sampling. Additionally, track volume measurements from high spatial-resolution datasets are more likely to reflect actual volumes [Lebel et al., 2012].

Fiber complexity is still present at high spatial resolution

The spatial resolution of the DTI-12 dataset presented here (130 microns isotropic) is at a much higher resolution than standard clinical diffusion imaging ($>10^3$ fold), and, to our knowledge, is the highest resolution diffusion imaging ever reported for the primate brain. Despite this unusually high resolution, tractography from the DTI-12 dataset was very inaccurate in complex fiber pathways. It seems that the 12-direction q-space sampling scheme, coupled with the diffusion tensor model that such sparse sampling necessitates, was simply incapable of accurately representing the intravoxel fiber geometry. This outcome suggests that the scale of fiber complexity is far smaller than the scale of currently feasible imaging voxels. Unless diffusion imaging resolution improves dramatically, it seems prudent to assume fiber complexity will always be present in some areas of the primate brain. In other words, it is not sufficient to use high spatial resolution as a means of globally eliminating intravoxel fiber complexity.

High q-space resolution can be insufficient for large voxels

It seems obvious that increased q-space sampling should lead to improved tractography, but this conclusion is not always true when it comes at the cost of decreased spatial resolution. For example, the DSI-257 dataset analyzed in this study was the most extensively sampled in q-space, but was not the most anatomically accurate. In particular, the DSI-257 dataset was prone to premature track termination (e.g., in the ILF and CB). Part of the issue is that large voxels

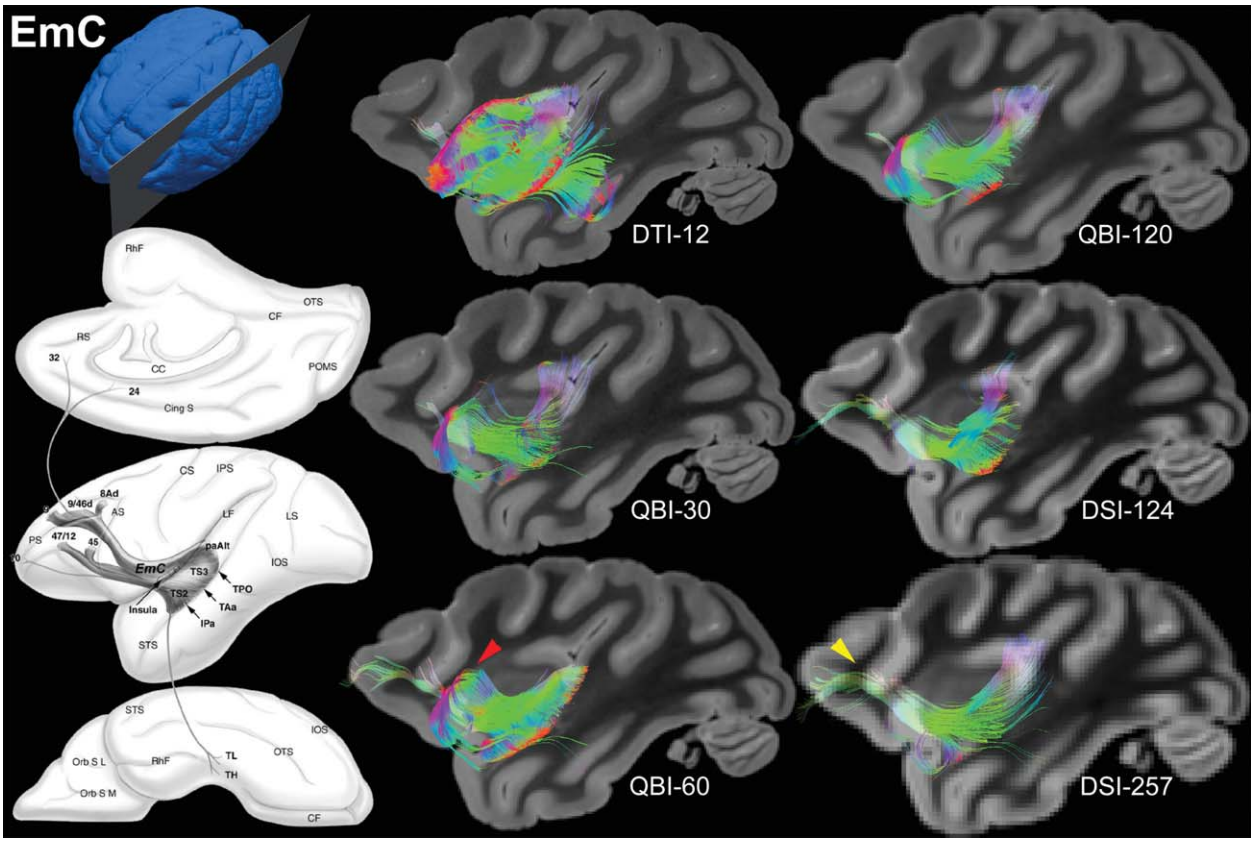

Figure 11.

Extreme capsule (EmC) tractography results. This "complex" pathway courses immediately deep to a sheet-like group of cortical U-fibers, which was a major source of erroneous stray fibers (e.g. QBI-30, red arrowhead) in all except the two DSI datasets. The superior anterior ramus extending into the dorsal prefrontal cortex was well represented in the QBI-30, DSI-124, and DSI-257 (yellow arrowhead) datasets, but was truncated in the other three datasets. [Color figure can be viewed in the online issue, which is available at wileyonlinelibrary.com.]

are more likely to contain multiple different white matter pathways, as well as parts of adjacent gray matter areas and/or fluid spaces. This effect is particularly pronounced when voxel size is large relative to the size of the white matter pathway being reconstructed. For example, the CB was only about four voxels wide in the DSI-257 dataset analyzed here. In this case, even extensive q-space sampling was incapable of accurately resolving underlying fiber geometry. It indicates that when voxels are large relative to the structure of interest, high q-space sampling may not be sufficient to resolve intravoxel fiber architecture.

Balance is best

In this study, the most anatomically accurate tractography results were achieved with a balance between spatial resolution and q-space sampling. The datasets that came the closest to representing known anatomy (QBI-60, QBI-120, and DSI-124) had small enough voxels to avoid major partial volume effects, and sufficient q-space sampling to resolve at least some degree of intravoxel fiber crossing. A similar analysis of in-vivo human tractography in the internal capsule and arcuate fasciculus seems to agree with these results, and also highlights the large track overlap differences that result from different acquisition and reconstruction strategies [Vos et al., 2013]. Based on these data, we suggest >30 gradient directions for accurate tractography of complex anatomy like the cortical association pathways studied here. This determination concurs with previous investigations on the effects of the number of gradient directions [Jones, 2004; Zhan et al., 2008, 2010], and is supported by our crossing fiber simulation data where errors in the crossing region were largely absent with >30 gradient directions. However, previous studies have shown that the optimal number of gradient direction depends on many factors including b-value, diffusion sampling pattern, and the spherical harmonic order used for Q-ball reconstruction [Tournier et al., 2013; White and Dale, 2009].

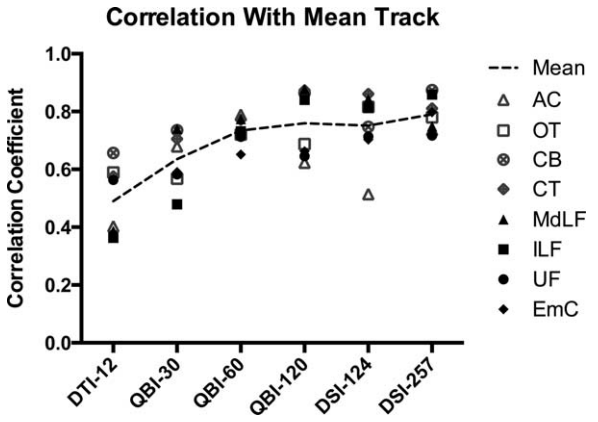

Figure 12.

Track density imaging (TDI) correlation results. A mean track was generated for each of the eight tracks analyzed in this study by averaging TDIs from all six protocols. Individual TDIs were then compared to the mean track using normalized cross correlation. Correlation results for "simple" pathways are shown with open (white) points, "intermediate" pathways with hatched (gray) points, and "complex" pathways with closed points (black). The average correlation coefficient across all eight pathways is indicated with a dotted line.

Relevance to Human Brain Mapping

We chose to image the macaque brain because its encephalization and overall structure provide a good model for the human brain. Previous tractography studies have shown that a many white matter pathways are similar in humans and macaques [Croxson, 2005; Parker et al., 2002], suggesting that the results presented here are directly relevant to human brain mapping. Although the spatial resolutions used for this study are much higher than a typical human dataset, it is important to consider differences in brain volume. The macaque brain is about 17-fold smaller than the human brain by volume [Herculano-Houzel, 2009], so voxels must be 17-fold smaller to achieve comparable structural resolution. Accounting for volumetric differences, the spatial resolutions reported here ($0.13-0.6$ mm) are comparable to spatial resolutions of $0.33-1.5$ mm in humans, which has considerable overlap with advanced ex-vivo studies of the human brain [McNab et al., 2009, 2013; Miller et al., 2011] and even some in-vivo human studies [Golay et al., 2002; Jeong et al., 2003; Kamali et al., 2009]. With human brain mapping initiatives moving toward higher field, multichannel receive coils, and stronger imaging gradients, it seems likely that clinical diffusion imaging resolution will continue to improve in the near future. With increasing resolution capabilities and ever expanding q-space sampling protocols, consideration of the tradeoffs explored in this manuscript will inevitably play a role in the future of human brain mapping with diffusion tractography.

CONCLUSIONS

In this study, we have shown that diffusion tractography results can vary widely with the choice of q-space sampling and spatial resolution, even when the tissue being imaged and the total acquisition time are held constant. We have also demonstrated that balancing acquisition time between q-space sampling and spatial resolution provides more anatomically accurate results than, for example, focusing solely on spatial resolution. One of the major limitations of our analyses, and of tractography in general, is the fact that it is largely qualitative. There is currently no quantitative method for assessing anatomic accuracy of tractography, and no universally accepted "gold standard" tractography protocol. Studies like this one will be essential for future attempts to generate gold standard tractography datasets for animal models and for the human brain. These results are particularly relevant for ex-vivo brain mapping studies where extended scan times are possible and high anatomic accuracy is required. Like other ex-vivo brain mapping methods (i.e., dissection, myelin-stained histology, tracer studies), diffusion tractography will certainly add to, rather than replace, previous anatomic knowledge. Perhaps the most important contribution of diffusion tractography will be to help integrate previous knowledge into a meaningful 3D map, and allow quantitative assessment of tract morphology and structural connectivity. We hope that our systematic analysis of different diffusion imaging protocols provides some insight into the best use of acquisition time for future brain mapping studies.

ACKNOWLEDGMENTS

The authors gratefully acknowledge the WNPRC for providing the specimens used in these analyses. Pathology and tissue distribution services at the WNPRC. We are grateful to Sally Gewalt and James Cook for assistance with the imaging pipelines and Gary Cofer for assistance in specimen preparation and scanning.

REFERENCES

Alexander DC, Hubbard PL, Hall MG, Moore EA, Ptito M, Parker GJM, Dyrby TB (2010): Orientationally invariant indices of axon diameter and density from diffusion MRI. Neuroimage 52:1374–1389.

Axer M, Grässel D, Kleiner M, Dammers J, Dickscheid T, Reckfort J, Hütz T, Eiben B, Pietrzyk U, Zilles K, Amunts K (2011): High-resolution fiber tract reconstruction in the human brain by means of three-dimensional polarized light imaging. Front Neuroinform 5:34.

Barmpoutis A, Jian B, Vemuri BC (2009): Adaptive kernels for multi-fiber reconstruction. Inf Process Med Imaging 21:338–349.

Basser PJ (1995): Inferring microstructural features and the physiological state of tissues from diffusion-weighted images. NMR Biomed 8:333–344.

Basser PJ (2002): Relationships between diffusion tensor and q-space MRI. Magn Reson Med 47:392–397.

Basser PJ, Pierpaoli C (1996): Microstructural and physiological features of tissues elucidated by quantitative-diffusion-tensor MRI. J Magn Reson B 111:209–219.

Basser PJ, Pajevic S, Pierpaoli C, Duda J, Aldroubi A (2000): In vivo fiber tractography using DT-MRI data. Magn Reson Med 44:625–632.

Callaghan PT, Eccles CD, Xia Y (1988): NMR microscopy of dynamic displacements: k-space and q-space imaging. J Phys E: Sci Instrum 21:820–822.

Catani M, Bodi I, Dell'Acqua F (2012): Comment on "The geometric structure of the brain fiber pathways". Science 337: 1605.

Croxson PL (2005): Quantitative Investigation of Connections of the Prefrontal Cortex in the Human and Macaque using Probabilistic Diffusion Tractography. J Neurosci 25:8854–8866.

D'Arceuil HE, Westmoreland S, de Crespigny AJ (2007): An approach to high resolution diffusion tensor imaging in fixed primate brain. Neuroimage 35:553–565.

Dawe RJ, Bennett DA, Schneider JA, Vasireddi SK, Arfanakis K (2009): Postmortem MRI of human brain hemispheres: T2 relaxation times during formaldehyde fixation. Magn Reson Med 61:810–818.

de Crespigny AJ, D'Arceuil HE, Dai G, Wang R, Kim Y, Mandeville JB, Wedeen VJ (2005): Comparison of in vivo and ex vivo Diffusion Spectrum Imaging (DSI) of Rat Brain. Proc Intl Soc Mag Reson Med 13:583.

Descoteaux M, Angelino E, Fitzgibbons S, Deriche R (2007): Regularized, fast, and robust analytical Q-ball imaging. Magn Reson Med 58:497–510.

Descoteaux M, Deriche R, Knösche TR, Anwander A (2009): Deterministic and probabilistic tractography based on complex fibre orientation distributions. IEEE Trans Med Imaging 28: 269–286.

Dyrby TB, Baaré WFC, Alexander DC, Jelsing J, Garde E, Søgaard LV (2011): An ex vivo imaging pipeline for producing high-quality and high-resolution diffusion-weighted imaging datasets. Hum Brain Mapp 32:544–563.

Farrell JAD, Landman BA, Jones CK, Smith SA, Prince JL, van Zijl PCM, Mori S (2007): Effects of signal-to-noise ratio on the accuracy and reproducibility of diffusion tensor imaging-derived fractional anisotropy, mean diffusivity, and principal eigenvector measurements at 1.5 T. J Magn Reson Imaging 26: 756–767.

Fillard P, Descoteaux M, Goh A, Gouttard S, Jeurissen B, Malcolm J, Ramirez-Manzanares A, Reisert M, Sakaie K, Tensaouti F, Yo T, Mangin J-F, Poupon C (2011): Quantitative evaluation of 10 tractography algorithms on a realistic diffusion MR phantom. Neuroimage 56:220–234.

Golay X, Jiang H, van Zijl PCM, Mori S (2002): High-resolution isotropic 3D diffusion tensor imaging of the human brain. Magn Reson Med 47:837–843.

Herculano-Houzel S (2009): The human brain in numbers: A linearly scaled-up primate brain. Front Hum Neurosci 3:31.

Hess CP, Mukherjee P, Han ET, Xu D, Vigneron DB (2006): Q-ball reconstruction of multimodal fiber orientations using the spherical harmonic basis. Magn Reson Med 56:104–117.

Jahanshad N, Zhan L, Bernstein MA, Borowski BJ, Jack CR, Toga AW, Thompson PM (2010): Diffusion tensor imaging in seven minutes: Determining trade-offs between spatial and directional resolution. In: Biomedical Imaging: From Nano to Macro, 2010 IEEE International Symposium, Rotterdam, Netherlands. pp 1161–1164.

Jeong E-K, Kim S-E, Parker DL (2003): High-resolution diffusion-weighted 3D MRI, using diffusion-weighted driven-equilibrium (DW-DE) and multishot segmented 3D-SSFP without navigator echoes. Magn Reson Med 50:821–829.

Jeurissen B, Leemans A, Tournier J-D, Jones DK, Sijbers J (2013): Investigating the prevalence of complex fiber configurations in white matter tissue with diffusion magnetic resonance imaging. Hum Brain Mapp 34:2747–2766.

Jones DK (2004): The effect of gradient sampling schemes on measures derived from diffusion tensor MRI: A Monte Carlo study. Magn Reson Med 51:807–815.

Kamali A, Kramer LA, Butler IJ, Hasan KM (2009): Diffusion tensor tractography of the somatosensory system in the human brainstem: Initial findings using high isotropic spatial resolution at 3.0 T. Eur Radiol 19:1480–1488.

Kim M, Ronen I, Ugurbil K, Kim D-S (2006): Spatial resolution dependence of DTI tractography in human occipito-callosal region. Neuroimage 32:1243–1249.

Lazar M, Alexander AL (2003): An error analysis of white matter tractography methods: Synthetic diffusion tensor field simulations. Neuroimage 20:1140–1153.

Le Bihan D, Poupon C, Amadon A, Lethimonnier F (2006): Artifacts and pitfalls in diffusion MRI. J Magn Reson Imaging 24: 478–488.

Lebel C, Benner T, Beaulieu C (2012): Six is enough? Comparison of diffusion parameters measured using six or more diffusion-encoding gradient directions with deterministic tractography. Magn Reson Med 68:474–483.

Lerch JP, Gazdzinski L, Germann J, Sled JG, Henkelman RM, Nieman BJ (2012): Wanted dead or alive? The tradeoff between in-vivo versus ex-vivo MR brain imaging in the mouse. Front Neuroinform 6:6.

Lo C-Y, Wang P-N, Chou K-H, Wang J, He Y, Lin C-P (2010): Diffusion tensor tractography reveals abnormal topological organization in structural cortical networks in Alzheimer's disease. J Neurosci 30:16876–16885.

McNab JA, Jbabdi S, Deoni SCL, Douaud G, Behrens TEJ, Miller KL (2009): High resolution diffusion-weighted imaging in fixed human brain using diffusion-weighted steady state free precession. Neuroimage 46:775–785.

McNab JA, Edlow BL, Witzel T, Huang SY, Bhat H, Heberlein K, Feiweier T, Liu K, Keil B, Cohen-Adad J, Tisdall MD, Folkerth RD, Kinney HC, Wald LL (2013): The Human Connectome Project and beyond: Initial applications of 300mT/m gradients. Neuroimage 80:234–245.

Miller KL, Stagg CJ, Douaud G, Jbabdi S, Smith SM, Behrens TEJ, Jenkinson M, Chance SA, Esiri MM, Voets NL, Jenkinson N, Aziz TZ, Turner MR, Johansen-Berg H, McNab JA (2011): Diffusion imaging of whole, post-mortem human brains on a clinical MRI scanner. Neuroimage 57:167–181.

Mori S, Crain BJ, Chacko VP, van Zijl, P. C. (1999): Three-dimensional tracking of axonal projections in the brain by magnetic resonance imaging. Ann Neurol 45:265–269.

Parker GJM, Stephan KE, Barker GJ, Rowe JB, MacManus DG, Wheeler-Kingshott CAM, Ciccarelli O, Passingham RE, Spinks RL, Lemon RN, Turner R (2002): Initial demonstration of in vivo tracing of axonal projections in the macaque brain and comparison with the human brain using diffusion tensor imaging and fast marching tractography. Neuroimage 15:797–809.

Rane S, Nair G, Duong TQ (2010): DTI at long diffusion time improves fiber tracking. NMR Biomed 23:459–465.

Schmahmann JD, Pandya D (2009): Fiber Pathways of the Brain. New York: Oxford University Press.

Schmahmann JD, Pandya DN, Wang R, Dai G, D'Arceuil HE, de Crespigny AJ, Wedeen VJ (2007): Association fibre pathways of the brain: Parallel observations from diffusion spectrum imaging and autoradiography. Brain 130:630–653.

Skare S, Andersson JL (2001): On the effects of gating in diffusion imaging of the brain using single shot EPI. Magn Reson Imaging 19:1125–1128.

Skudlarski P, Jagannathan K, Anderson K, Stevens MC, Calhoun VD, Skudlarska BA, Pearlson G (2010): Brain connectivity is not only lower but different in schizophrenia: A combined anatomical and functional approach. Biol Psychiatry 68:61–69.

Sundaram SK, Kumar A, Makki MI, Behen ME, Chugani HT, Chugani DC (2008): Diffusion tensor imaging of frontal lobe in autism spectrum disorder. Cereb Cortex 18:2659–2665.

Tournier J-D, Calamante F, Connelly A (2013): Determination of the appropriate b value and number of gradient directions for high-angular-resolution diffusion-weighted imaging. NMR Biomed 26:1775–1786.

Tuch DS (2004): Q-ball imaging. Magn Reson Med 52:1358–1372.

Tuch DS, Reese TG, Wiegell MR, Makris N, Belliveau JW, Wedeen VJ (2002): High angular resolution diffusion imaging reveals intravoxel white matter fiber heterogeneity. Magn Reson Med 48:577–582.

Tuch DS, Reese TG, Wiegell MR, Wedeen VJ (2003): Diffusion MRI of complex neural architecture. Neuron 40:885–895.

Vos SB, Aksoy M, Han Z, Holdsworth SJ, Seeger C, Julian M, Brost A, Leemans A, Bammer R (2013): HARDI and fiber tractography at 1 mm isotropic resolution. In: Proc Intl Soc Mag Reson Med, Salt Lake City, Utah, USA. p 842.

Wedeen VJ, Hagmann P, Tseng W-YI, Reese TG, Weisskoff RM (2005): Mapping complex tissue architecture with diffusion spectrum magnetic resonance imaging. Magn Reson Med 54: 1377–1386.

Wedeen VJ, Wang RP, Schmahmann JD, Benner T, Tseng WYI, Dai G, Pandya DN, Hagmann P, D'Arceuil H, de Crespigny AJ (2008): Diffusion spectrum magnetic resonance imaging (DSI) tractography of crossing fibers. Neuroimage 41:1267–1277.

Wedeen VJ, Rosene DL, Wang R, Dai G, Mortazavi F, Hagmann P, Kaas JH, Tseng W-YI (2012): The geometric structure of the brain fiber pathways. Science 335:1628–1634.

White NS, Dale AM (2009): Optimal diffusion MRI acquisition for fiber orientation density estimation: An analytic approach. Hum Brain Mapp 30:3696–3703.

Yamamoto A, Miki Y, Urayama S, Fushimi Y, Okada T, Hanakawa T, Fukuyama H, Togashi K (2007): Diffusion tensor fiber tractography of the optic radiation: Analysis with 6-, 12-, 40-, and 81-directional motion-probing gradients, a preliminary study. AJNR Am J Neuroradiol 28:92–96.

Yeh F-C, Tseng W-YI (2013): Sparse solution of fiber orientation distribution function by diffusion decomposition. PLoS ONE 8:e75747.

Yeh F-C, Wedeen VJ, Tseng W-YI (2011): Estimation of fiber orientation and spin density distribution by diffusion deconvolution. Neuroimage 55:1054–1062.

Zhan L, Chiang MC, Barysheva M, Toga AW, de Zubicaray GI, Meredith M, Wright MJ, Thompson PM (2008): How many gradients are sufficient in high-angular resolution diffusion imaging (HARDI)?. In: 13th Annual Meeting of the Organization for Human Brain Mapping (OHBM), Melbourne, Australia.

Zhan L, Leow AD, Jahanshad N, Chiang M-C, Barysheva M, Lee AD, Toga AW, McMahon KL, de Zubicaray GI, Wright MJ, Thompson PM (2010): How does angular resolution affect diffusion imaging measures? Neuroimage 49:1357–1371.

Zhan L, Franc D, Patel V, Jahanshad N, Jin Y, Mueller BA, Bernstein MA, Borowski BJ, Jack CR, Toga AW, Lim KO, Thompson PM (2012a): How do spatial and angular resolution affect brain connectivity maps from diffusion MRI?. In: Proc IEEE Int Symp Biomed Imaging, Barcelona, Spain. pp 1–6.

Zhan L, Jahanshad N, Ennis DB, Jin Y, Bernstein MA, Borowski BJ, Jack CR, Toga AW, Leow AD, Thompson PM (2012b): Angular versus spatial resolution trade-offs for diffusion imaging under time constraints. Hum Brain Mapp.